HHS Public Access

Author manuscript

J Thorac Oncol. Author manuscript; available in PMC 2024 July 01.

Published in final edited form as:

J Thorac Oncol. 2023 July ; 18(7): 882–895. doi:10.1016/j.jtho.2023.03.014.

Histone deacetylase 6 inhibition exploits selective metabolic vulnerabilities in LKB1 mutant, KRAS driven non-small cell lung cancer

Hua Zhang[1,2,*], **Christopher S. Nabel**[3,4,*], **Dezhi Li**[2], **Ruth Í. O'Connor**[5], **Caroline R. Crosby**[3], **Sarah M. Chang**[2], **Yuan Hao**[6], **Robyn Stanley**[5], **Soumyadip Sahu**[2], **Daniel S. Levin**[2], **Ting Chen**[2], **Sittinon Tang**[2], **Hsin-Yi Huang**[2], **Mary Meynardie**[2], **Janaye Stephens**[2], **Fiona Sherman**[2], **Alison Chafitz**[2], **Naoise Costelloe**[5], **Daniel A. Rodrigues**[7], **Hilda Fogarty**[5], **Miranda G. Kiernan**[5], **Fiona Cronin**[5], **Eleni Papadopoulos**[2], **Magdalena Ploszaj**[2], **Vajira Weerasekara**[4], **Jiehui Deng**[2], **Patrick Kiely**[5,8], **Nabeel Bardeesy**[4], **Matthew G. Vander Heiden**[3,9], **Triona Ni Chonghaile**[7], **Catríona M. Dowling**[5,8,**], **Kwok-Kin Wong**[2]

[1]Department of Medicine, Division of Hematology/Oncology, University of Pittsburgh School of Medicine, UPMC Hillman Cancer Center, Pittsburgh, PA, 15232, USA

[2]Division of Hematology & Medical Oncology, Laura and Isaac Perlmutter Cancer Center, New York University Langone Medical Center, New York, NY, USA

[3]Koch Institute for Integrative Cancer Research, MIT, Cambridge, MA

[4]Massachusetts General Hospital Cancer Center, Boston, MA, USA

[5]School of Medicine, University of Limerick, Limerick, Ireland

[6]Applied Bioinformatics Laboratories, Office of Science and Research, New York University Grossman School of Medicine, New York, New York, USA

[7]Department of Physiology and Medical Physics, Royal College of Surgeons in Ireland, Dublin, Ireland

[8]Health Research Institute, University of Limerick, Limerick, Ireland

[9]Dana-Farber Cancer Institute, Harvard Medical School, Boston, MA, USA

Abstract

[**]**To whom correspondence should be addressed.** Dr. Catríona Dowling, School of Medicine, University of Limerick, Limerick, Ireland, Catriona.Dowling@ul.ie.

[*]Joint first authors (Contributed equally to manuscript)

Conflicts of Interest: Dr. Wong is a founder and equity holder of G1 Therapeutics and has sponsored research agreements with MedImmune, Takeda, TargImmune, Bristol-Myers Squibb (BMS), Mirati, Merus, and Alkermes, and consulting and sponsored research agreements with AstraZence, Janssen, Pfizer, Novartis, Merck, Ono, and Array. N.G.S is a founder, science advisory board member and equity holder in Gatekeeper, Syros, Petra, C4, B2S, and Soltego. Dr. Ni Chonghaile reports other from Abbvie, outside the submitted work; Dr. Vander Heiden reports personal fees from Agios Pharmaceuticals, personal fees from iTeos Therapeutics, personal fees from Auron Therapeutics, personal fees from Sage Therapeutics, personal fees from Droia Ventures, outside the submitted work; Dr. Nabel reports other (royalties) from Cambridge Epigenetix, other (royalties) from Life Technologies, other (stock ownership) from Opko Health, outside the submitted work; Dr. Bardeesy reports grants from NIH, during the conduct of the study; Dr. Kiely reports grants and non-financial support from Enterprise Ireland Academic/Industry co-fund innovation partnership research grant, (where BD Biosciences are an Industry Partner/Co-applicant) outside the submitted work; The other authors declare no potential conflicts of interest.

Introduction: In *KRAS*-mutant non-small lung cancer (NSCLC), co-occurring alterations in LKB1 confer a negative prognosis compared to other mutations such as TP53. LKB1 is a tumor suppressor that coordinates several signaling pathways in response to energetic stress. Our recent work on pharmacologic and genetical inhibition of HDAC6 demonstrated impaired activity of numerous enzymes involved in glycolysis. Based on these prior findings, we explored the therapeutic window for HDAC6 inhibition in metabolically-active *KRAS*-mutant lung tumors.

Experimental Design: Using cell lines derived from mouse autochthonous tumors bearing the KRAS/LKB1 (KL) and KRAS/TP53 (KP) mutant genotypes to control for confounding germline and somatic mutations in human models, we characterize the metabolic phenotypes at baseline and in response to HDAC6 inhibition. The impact of HDAC6 inhibition was measured on cancer cell growth *in vitro* and on tumor growth *in vivo*.

Results: Surprisingly, KL-mutant cells demonstrated reduced levels of redox-sensitive cofactors at baseline. This associated with increased sensitivity to pharmacologic HDAC6 inhibition with ACY-1215 and blunted ability to increase compensatory metabolism and buffer oxidative stress. Seeking synergistic metabolic combination treatments, we found enhanced cell killing and anti-tumor efficacy with glutaminase inhibition in KL lung cancer models *in vitro* and *in vivo*.

Conclusions: Exploring the differential metabolism of KL and KP mutant NSCLC, we identified decreased metabolic reserve in KL mutant tumors. HDAC6 inhibition exploited a therapeutic window in KL NSCLC based on a diminished ability to compensate for impaired glycolysis, nominating a novel strategy for treatment of *KRAS*-mutant NSCLC with co-occurring LKB1 mutations.

Keywords

HDAC6; KRAS; LKB1; TP53; non-small cell lung cancer; glycolysis; glutaminase inhibition; oxidative stress

Introduction

Histone deacetylase 6 (HDAC6) is important for cancer progression and is a therapeutic target [1], with ongoing clinical trials assessing the use of HDAC6-selective inhibitors (HDAC6i) [1–3]. We reported a new role for HDAC6 in the regulation of glycolysis [4], demonstrating that HDAC6 binds to and deacetylates key enzymes involved in this metabolic pathway. Treatment of triple negative breast cancer (TNBC) cells with a novel HDAC6i impaired glycolysis and reduced tumor growth in TNBC mouse models. This unexpected role for HDAC6 in regulation of glucose metabolism creates an opportunity for the discovery of new combination regimens with HDAC6 inhibitors to treat cancer.

KRAS is the most common molecular alteration in lung adenocarcinoma, the predominant subtype of non-small cell lung cancer (NSCLC), and is present in approximately 30% of these patients. In contrast with other frequently mutated oncogenes in NSCLC, KRAS has been a challenging molecule to target. While small molecule inhibitors of the G12C allele have recently gained approvals, this only captures a minority of KRAS mutations and an informed understanding of disease biology is needed to identify additional treatment options. KRAS mutations often co-occur with secondary mutations in tumor suppressors

such as TP53 (co-mutated ~ 46%) and LKB1 (co-mutated ~ 10%) and the presence of these co-existing genetic mutations impacts clinical response to treatment [5, 6]. KRAS/TP53 (KP) co-altered cancers demonstrate good responses to anti-PD-1 immunotherapy, while KRAS/LKB1 (KL) NSCLCs have inferior responses [7]. The mechanism(s) responsible for the differential biology associated with these responses remains poorly understood. A greater understanding of these differences may inform the design of new treatment strategies.

LKB1 is a serine-threonine kinase that phosphorylates numerous downstream signaling kinases to facilitate their activation, including the energy sensor AMP Kinase (AMPK). Through modulation of AMPK activity, LKB1 status impacts processes including autophagy and mitochondrial fission that are critical for how the cell responds to energetic stress [8]. By facilitating catabolic cellular processes and suppressing anabolic pathways, AMPK enables the cell to adapt to nutrient stress conditions. Prior work has demonstrated that mitochondrial remodeling and autophagy remain impaired in mouse models of KL lung cancer [9, 10], providing a biological rationale for why these cells may be sensitive to metabolic perturbations.

Given that HDAC6 inhibition impairs glycolysis, we explored the differential therapeutic index between two genotypes of KRAS-mutant (KL versus KP) NSCLC. We characterize phenotypes linked to central carbon metabolism using cells derived from KL and KP mouse models, and observe a diminished reserve for metabolic perturbations in the KL genotype with HDAC6 disruption. This correlates with enhanced sensitivity to pharmacologic inhibition of HDAC6 in the KL genotype. With metabolic correlates of HDAC6i converging on oxidative stress, we further explore synergy between HDAC6i's and glutaminase inhibitors (GLSi) as a potential new combination regimen for genotype-selected KL NSCLC patients, and identify a metabolic rationale for exploration of further combination strategies.

Results

Characterization of the metabolic phenotype of KRAS/LKB1 and KRAS/TP53 NSCLC

Unlike human cell lines, which harbour confounding germline and somatic mutations, genetically engineered mouse models (GEMMs) provide a valuable tool for studying the biological differences between KRAS subsets in a controlled manner. We examined numerous metabolic phenotypes of KL and KP NSCLC using murine cell lines derived from GEMMs with either a KRAS/LKB1 or KRAS/TP53 background. Despite the more aggressive nature of the KL subtype *in vivo*, at baseline, we found no difference in the growth rate between the KL and KP cells (Figure 1A). Glucose, lactate and glutamine are key metabolites cells exchange with their environment, but we observed no differences in glucose or glutamine consumption rates or in the rate of lactate production between the KL and KP cell lines (Figure 1B). Profiling polar metabolite abundance by liquid chromatography-mass spectrometry (LC/MS) demonstrated distinct segregation of the KL and KP cell lines by unsupervised hierarchical clustering analysis (Figure S1A). Variable importance projection identified differentially-enriched metabolites (Figure S1B), but few metabolites were significantly different in the unperturbed state (Figure S1C). In order to investigate whether KP or KL cells displayed a greater reliance on glucose and/or glutamine metabolism, we measured cell growth under conditions of selective nutrient withdrawal.

Interestingly, no difference was observed in the growth rate of KP or KL cells following glucose withdrawal (Figure 1C); however, glutamine deprivation resulted in reduced KL cell proliferation compared to KP cells (Figure 1C). Reduced oxygen consumption rate (OCR) was also observed in the KL cell lines (Figure 1D). Oxidative phosphorylation along with several other metabolic reactions in tumors are fuelled by the oxidative and reductive power of nicotinamide adenine dinucleotide (NAD) cofactors, in both phosphorylated (NADP+/NADPH) and unphosphorylated (NAD+/NADH) forms. Here, we observed a reduction in all NAD cofactors in the KL cells compared to the KP cells (Figure 1E). Similarly, there was also a decrease in total, oxidised and reduced levels of the antioxidant glutathione (GSH/GSSG) in the KL cells (Figure 1F).

We next sought to determine whether observations that support metabolic differences between KRAS-subsets of NSCLC are also observed in human patient samples. Since the metabolic parameters of enzymatic pathways are not often captured at the level of RNA expression, we analysed a recently published dataset on the proteogenomic characterization of 101 cases of lung adenocarcinoma [11]. The clinical cohort included 33 KRAS-positive cases, with 12 containing co-occurring LKB1 alterations and 21 LKB1-wild type. We evaluated differential enrichment of protein expression assessed by peptide fragment LC-MS. Consistent with known LKB1 mutational status, LKB1 expression was decreased in the KRAS/LKB1-comutant cohort compared to KRAS mutant, LKB1-wild type (Figure S2A). By contrast, the KRAS/LKB1-comutant cohort had increased expression of carbamoyl phosphate synthetase-1 (CPS1), consistent with prior reports (Figure S2B) [12]. These controls provided confidence in the validity of the dataset with respect to the biology of KRAS-mutant tumors. We then evaluated the differential protein enrichment across the proteomic dataset (Figure S2C). Within the group of hits with differential expression, there was a preponderance of metabolic genes based on annotation in the Kyoto Encyclopedia of Genes and Genomes (KEGG) Pathway database. Upon further sub-grouping, the majority of differentially-enriched proteins were members of the oxidative phosphorylation pathway (Figure S2D). Other pathway members included numerous subunits of the ATP synthase complex (Complex V) of the electron transport chain, along with other components involved in electron transfer (Figure S2E). Protein expression was uniformly increased in the KRAS/LKB1-comutant cohort. This is consistent with prior reports of diminished mitophagy as a result of decreased AMP Kinase (AMPK) signalling [9]. While that study explored the impacts of impaired mitochondrial homeostasis on apoptotic cell death, the consequences for impaired cellular respiration are consistent with our *in vitro* experimental findings.

Taken together, our findings of decreased oxygen consumption rate and redox cofactor availability suggest potential diminished reserve of KL cells to survive metabolic perturbations.

Enhanced sensitivity to HDAC6 inhibition in KRAS/LKB1-comutant NSCLC

We have recently defined metabolic impacts of HDAC6 inhibition through hyperacetylation of the glycolytic enzymes aldolase, enolase, lactate dehydrogenase A (LDHA) and glyceraldehyde-3-phosphate dehydrogenase (GAPDH) [13]. We observed increased expression in three of these glycolytic enzymes in the KL cells compared to the KP cells by RNA-

sequencing (Figure S3A). Given this, along with the potential impaired ability of KL cells to adjust to metabolic perturbations, we investigated the sensitivity of KL and KP models to HDAC6 inhibition. We first examined the effect of the HDAC6i, ACY1215, on a panel of KL and KP murine cell lines and found enhanced sensitivity in the KL genotype (KL IC_{50} 3.4–1.9 μM; KP IC_{50} 12.3–14.2 μM) (Figure 2A). This differential sensitivity was observed with a second, chemically-distinct HDAC6 inhibitor, BAS-2 (Figure 2B). Moreover, we confirmed the sensitivity of KL and KP cells to HDAC6 inhibitors in three-dimensional (3D) spheroids. Again, there was a significant reduction in 3D spheroid formation in the KL condition when treated with ACY1215 and BAS-2 (Figure 2C,D & S3D, E), but not in the KP condition (Figure 2E, F & S3F, G). Human NSCLC cells harboring either LKB1 or TP53 mutations were evaluated to validate the findings in mouse cells, and similar results were observed (Figure S3B, C).

We next sought to assess whether HDAC6 inhibition would have superior efficacy in KL tumors in comparison to KP tumors. We first evaluated the baseline metabolic parameters of syngeneic KL and KP tumors derived from subcutaneous implantation of murine KLA and KPA cancer cell lines and found decreased levels of NAD co-factors and glutathione species (Figure 2G, 2H). With these established syngeneic KL and KP mouse models recapitulating the relevant metabolic features seen *in vitro*, we treated tumor-bearing mice with single agent ACY1215. Following 7 days of treatment, a significant reduction in tumor volume was noted in the KL but not the KP mouse model (Figure 2I, J, S4A, B). These findings confirm that KRAS driven NSCLC with a co-mutation of LKB1 are more sensitive to HDAC6 inhibition *in vitro* and *in vivo*.

HDAC6 inhibition impairs metabolic adaptations in KL cells

Based on the differential sensitivity to HDAC6i, next we sought to characterize the metabolic consequences of HDAC6 inhibition in both KRAS-mutant NSCLC genotypes. Increased glucose and glutamine utilization, along with increased lactate production was observed in the KP cells following treatment with ACY1215 (Figure 3A). However, no alterations in nutrient utilization were observed in the KL cells following drug treatment (Figure 3A). There were no changes in OCR identified in either genotype following drug treatment (Figure 3B); however, there was an increase in all NAD cofactors in both KP and KL cell lines treated with ACY1215 compared to control (Figure 3C). Reduced and oxidized glutathione were preserved in the KP cells, but decreased in the KL cells (Figure 3D), corresponding with a reduction in the expression of the GCLC enzyme in drug treated KL cells (Figure S5A).

To assess potential perturbations across a larger panel of metabolites, we analyzed metabolites from cells from both KP and KL backgrounds treated with ACY1215 versus vehicle control by LC/MS. Using principal component analysis to assess metabolite differences between genotypes, we found that the KP vehicle condition clustered separately from the KP ACY1215 treatment, and that KP cells treated with ACY1215 showed increased clustering with both KL vehicle and ACY1215 treated conditions (Figure S5B). Consistent with this observation, unsupervised hierarchical clustering analysis of metabolites measured from the KP background demonstrated distinct segregation of ACY1215 versus

vehicle treatment conditions (Figure S5C) but not in the KL background (Figure S5D), suggesting a genotype-specific inability to coordinate a differential metabolic response to drug treatment. To identify pertinent metabolic changes, we performed variable importance projection analysis of ACY1215 treatment versus vehicle in cells from both genetic backgrounds (Figure 3E, 3F). There were 10 common metabolites between the two backgrounds (Figure 3G). Glucose-6-phosphate was reduced, indicating HDAC6 inhibition leads to reduced glucose capture (Figure 3H). By contrast, 3-phosphoglycerate and phosphoenolpyruvate were increased (Figure 3H), with a greater magnitude of increase in the KP condition potentially indicating greater capacity for maintaining levels of precursors for downstream processes including serine and pyruvate formation. ACY1215 treatment resulted in increases in carnitine and acylcarnitine species in the KP cells but not KL cells (Figure S5E), consistent with prior reports of impaired beta-oxidation of fatty acids in KP cells to maintain energy homeostasis [10]. Fatty acid synthesis is supported by glycolysis and the conversion of pyruvate to acetyl-CoA for citrate synthesis. Given our prior identification of a selective requirement for pyruvate dehydrogenase (PDHB) in KL but not KP cells [14], we examined citrate as a metabolite linking glycolysis and fatty acid synthesis. Upon ACY1215 treatment, citrate increased in the KP condition compared to vehicle (Figure 3H). By contrast, there was no citrate increase in the KL condition. Together, this metabolomic analysis suggested that ACY1215 treatment results in changes in metabolite levels in numerous downstream biosynthetic pathways.

Combination of HDAC6 and glutaminase inhibitors enhances efficacy in KL models in vivo and in vitro.

With our prior demonstration that HDAC6 inhibition impairs glycolysis, and our current findings of differential response based on LKB1 status, we sought synergistic treatment strategies rooted in a complementary metabolic liability. Glutaminase (GLS) converts glutamine to glutamate, the precursor for GSH synthesis and a carbon contributor to the TCA cycle [15, 16]. Given the convergence of phenotypes suggesting sensitivity to oxidative stress in KL models treated with HDAC6i's, we explored the potential of inhibiting glutamine use in combination with HDAC6 inhibitors. There was a significant shift in the IC_{50} value when the GLS inhibitor, CB-839 was combined with ACY1215 in the KL cell lines (Figure 4A & S6A), a result not seen in the KP cell lines (Figure 4B). This combination regimen remained effective in 3D spheroids with consistent reduction in the ability of KL cells to form spheroids in the combination group when compared to treatment with either single agent alone (Figure 4C,D). Similar to the 2D culture data, minimal effect of single agent or combination treatment in the size of the KP spheroids was observed (Figure 4E,F).

Finally, we examined the efficacy of this combination regimen in KL syngeneic murine models. Following 2 weeks of treatment, we observed a significant reduction in tumor volume in mice treated with either ACY1215 or CB-839 as a single agent (Figure 4G). Consistently, the anti-tumor effect was further enhanced when combining ACY1215 and CB-839 (Figure 4G, S6B). We observed similar anti-tumor effects with our combination strategy in a xenograft model with the A549 (KL) human cell line, which harbours KRAS/LKB1 mutations (Figure S6C). By immunohistochemistry, we observed a marked increase

in caspase-3 and a decrease in Ki67 expression in our combination treatment compared to vehicle controls and single-drug treatment arms (Figure S6D). Collectively, these data suggests that HDAC6 inhibition synergizes with glutaminase inhibition to exploit a therapeutic window between KL and KP tumours based on differential ability to coordinate cellular metabolism.

Discussion

There remains a need for improved treatment of KRAS-mutant lung cancer, particularly in cases with secondary mutations in LKB1 given the limited responses to standard therapies. Here, we demonstrate a diminished metabolic reserve for buffering oxidoreductive stress in KL NSCLC that is associated with increased sensitivity to HDAC6 inhibition. HDAC6 inhibition resulted in decreased levels of glutathione in the KL condition, whereas KP cells were able to increase consumption of glucose and glutamine, demonstrating increased expansion of NAD cofactor levels and preservation of glutathione stores. Based on this finding, we explored the combination of HDAC6i and GLSi and found further sensitization in the KL models, both *in vitro* and *in vivo.* Collectively, these findings demonstrate a differential therapeutic index in KL NSCLC compared to KP NSCLC, which might be exploited as a new treatment strategy for KL mutant NSCLC patients.

This study expands upon our prior demonstration that HDAC6 inhibition impairs glycolytic activity through the acetylation of numerous glycolytic enzymes [13]. Given the metabolic changes associated with gain-of-function mutations in KRAS and loss-of-function mutations in LKB1, we evaluated the role for HDAC6 inhibition in the different pertinent subsets of KRAS-mutant NSCLC. We have previously evaluated the consequences of KRAS mutation in different tissues of origin, specifically lung versus pancreas [16]. In that study, we found that KRAS-mutant lung cancers demonstrated increased glucose contribution to the TCA cycle as opposed to glutamine. This contrasted with pancreatic tumors, which have more robust utilization of glutamine for sustaining the TCA cycle [17]. Both studies were performed in genetically-engineered mouse models bearing secondary mutations in TP53, which retain wild-type LKB1 status. In our current study, we have found that glucose consumption increases in KP lung cancer models when challenged with HDAC6 inhibition. Given that activating KRAS mutations also increase glucose utilization [18], it is likely that intact LKB1 status is required for this adaptation. By contrast, the KL model with LKB1 inactivation was not able to increase glucose consumption when challenged with HDAC6 inhibition. This increased sensitivity to a pharmacologic perturbation that diminishes glycolytic activity implies that LKB1 inactivation blunts the ability of KRAS to coordinate the metabolic response of the cancer cell. This increased dependency of glucose anaplerosis to the TCA is consistent with our prior report of the selective dependency for PDHB knockdown in the KL model [14].

Glutaminase inhibition with CB-839 has been studied in combination with frontline carboplatin, pemetrexed and pembrolizumab in a randomized, placebo-controlled manner (NCT04265534). This trial was advanced with the rationale of glutamate depletion via glutaminase inhibition and xCT-mediated transport [19], which assumes a cysteine-rich extracellular environment [20]. Our results suggest other pathways such as glycolysis may

have compensatory effect in the setting of metabolic perturbation of decreased TCA cycle and glutathione metabolism. Given our prior observations regarding glucose utilization in KRAS-mutant lung cancer [16], ongoing work is needed to better define selective metabolic strategies in these oncogenotypes.

Unlike other oncogenes in NSCLC such as EGFR and ALK, KRAS has historically been considered 'undruggable' due to structural and biochemical obstacles [21]. While recent advances have led to the development of the first targeted KRAS-G12C inhibitors, Sotorasib and Adagrasib [22], these drugs only benefit a subset of NSCLC patients. Furthermore, on-target and bypass activation have both been described as adaptive mechanisms of resistance seen with both agents [23, 24]. Both for patients with non-targetable alleles and also those patients with relapsed disease following G12C inhibition, it is important that efforts continue to discover novel combination regimens anchored by biological studies of KRAS biology and the role of its co-occurring mutations. To this end, a strength in the use of genetically-engineered mouse models is the ability to control for genetic heterogeneity that confounds model systems derived from human tissue. Using these isogenic mouse models, our findings illustrate the importance of glycolysis as a therapeutic target in the KL background as a building block for further combination strategies. Our study establishes that this metabolic vulnerability can be further exploited through the addition of a GLSi, offering a novel combination regimen for a group of patients with an urgent clinical need.

Material and Methods

Cell Culture

The KRAS/LKB1 (KL) and KRAS/TP53 (KP) cells were isolated from KRAS/LKB1$^{+/LSL\text{-}G12D}$;LKB1$^{fl/fl}$) or KRAS/TP53 (KRAS$^{+/LSL\text{-}G12D}$;TP53$^{fl/fl}$) genetically engineered mouse models (GEMS). H23 and H358 cells were purchased from American Type Culture Collection (ATCC). All cell lines were maintained in RPM1-1640 medium (Sigma-Aldrich) and supplemented with 10% (v/v) fetal bovine serum (Sigma-Aldrich), 1% (v/v) L-Glu (Sigma-Aldrich) and 1% (v/v) pencillin/streptomycin (Sigma-Aldrich). For experiments with glutamine and glucose withdrawal, RPMI-1640 was reconstituted from powder formulation without glucose/glutamine (Gibco) and supplemented with Sodium Bicarbonate (2g/L) and selective replacement of glucose (2g/L) and/or glutamine (300 mg/L) as indicated. ACY1215 was purchased from Cayman Chemical and Selleck Chemicals. BAS-2 was synthesised in Dr. Triona Ni Chonghaile Lab. CB-839 was purchased from Selleck Chemicals.

Cell Viability Assay

Cells were treated with drugs for indicated time points and cell viability was detected using the cell counting kit – 8 (Sigma – Aldrich) according to the manufactures instructions.

Population Doublings

50,000 cells were plated in 5 cm and allowed to adhere overnight. On the following day, reference condition counted on Multisizer3 (Beckman Coulter) to determine population index. Media was exchanged into fresh RPMI-1640 with indicated concentrations of drug

or vehicle control and allowed to grow for 72 hours before measuring final cell counts. Population doublings per day determined from the equation $r=\ln(P_{final}/P_0)/3$.

3D Cell Culture

Individual wells of a 12 well plate were coated with Matrigel (Corning) and placed in an incubator at 37°C for 30 min. A total of 10,000 cells/ml were resuspended in RPMI supplemented with 2% Matrigel. Cells were placed in Matrigel – coated well for 15 min at 37°C, after which RPMI supplemented with 2% Matrigel was added to the cultures. Cells were treated with indicated drugs after 24 hours. Cells were maintained in culture for 7 days in an incubator at 37°C, 5% CO_2, and cultures were imaged every 48 hours with a Olympus cellSens Dimension 1.12.

Human Tumor Proteomic Data Analysis

Processed and normalized total proteomic data was downloaded from the Clinical Proteomic Tumor Analysis Consortium study of lung adenocarcinoma (Supplemental Table 3A from that study) [11]. The dataset was filtered to remove all normal tissue samples and KRAS-wild type tumors. KRAS-mutant tumors were further stratified based on STK11 (LKB1) mutation status (mutant versus wild type). Data was then transferred to GraphPad Prism for analysis by parametric unpaired T-test (multiple per row). Multiple comparison testing was performed with false discovery correction by the method of Benjamini, Krieger and Yekutieli and false discovery rate of 5%.

Animal Studies

All animal studies were reviewed and approved by the Institutional Animal Care and Use Committee (IACUC) at NYU Grossman School of Medicine. Six-week old C57BL/6 (B6) mice were purchased from Jackson Laboratory (Stock No: 000664). All mice were maintained in accordance with NYU Grossman School of Medicine on the care, welfare, and treatment of laboratory animals. All experiments met or exceeded the standards of the Association for the Assessment and Accreditation of Laboratory Animal Care, International (AAALAC), the United States Department of Health and Human Services, and all local and federal animal welfare laws.

For treatment studies, 1.0×10^6 KL or KP cells were subcutaneously inoculated into the flanks of B6 mice. The mice had a tumor size of approximately 100 mm^2 before randomization of treatment. Mice were treated daily with either vehicle, ACY1215 (50 mg/kg), CB-839 (200 mg/kg) or combined ACY1215 and CB-839. Caliper was used to measure tumor volume [(length × $width^2$)/2]. Similarly, for the human cell line xenograft study, 1.0×10^6 A549 cells were subcutaneously inoculated into the flanks of nude mice. Once the tumor size reached to approximately 100 mm^2, the mice were randomized to four treatment group as described above.

Histology and Immunohistochemistry

Tumor samples were fixed overnight in 4% paraformaldehyde (or neutral buffered formalin), and then processed through graded ethanols, xylene and into paraffin on a Leica Peloris

automated tissue processor. Five-micron thick sections were prepared and either stained with hematoxylin (Leica, 3801575) and eosin (Leica, 3801619) on a Leica ST5020 stainer or immunostained on a Leica BondRX automated stainer, according to the manufacturer instructions. In brief, tissues for immunostaining underwent deparaffinization online followed by epitope retrieval for 20 minutes at 100° with Leica Biosystems ER2 solution (pH9, AR9640) and endogenous peroxidase activity blocking with H_2O_2. Sections were incubated with primary antibodies against Ki67 (Abcam, Cat #ab16667; clone SP6) at a 1:100 dilution or against cleaved caspace 3 (Cell Signaling Technologies, Cat #9579; clone D3E9) at a dilution of 1:200 for 30 minutes at room temperature. Primary antibodies were detected with anti-rabbit HRP-conjugated polymer and 3,3'-diaminobenzidine (DAB) substrate that are provided in the Leica BOND Polymer Refine Detection System (Cat # DS9800). Following counter-staining with hematoxylin, slides were scanned at 40X on a Leica AT2 whole slide scanner (Aperio Image Library v12.0.16, Leica Biosystems) and the image files uploaded to the NYUGSoM's OMERO Plus image data management system (Glencoe Software).

RNA Extraction and Bulk-RNA Sequencing Analysis

Cell pellets were collected and then subjected to total RNA extraction using RNeasy Plus MiniKit (QIAGEN, Cat#74136) according to the manufacturer's instructions. Read qualities were evaluated using FASTQC (Babraham Institute) and mapping to GRCm38 (GENCODE M25) reference genome using STAR program [25]. with default parameters. Read counts, TPM and FPKM were calculated using RSEM program [26]. Identification of differentially expressed genes was performed using DESeq2 in R/Bioconductor (R version 4.0.4). All plots were generated using customized R scripts. Additionally, a customized gene set associated with indicated metabolic pathways were established and heatmap was generated based on their normalized expression values.

Extracellular Flux Assay

The bioenergetic function of cells in response to drug treatments was determined using a Seahorse Bioscience X96 Extracellular Flux Analyzer (Seahorse Bioscience). 5,000 Cells were seeded in specialized V7 Seahorse tissue culture plates (Agilent, 102601 – 100) and allowed to adhere overnight. In cases of ACY1215 pretreatment, cells were incubated in drug versus vehicle control for indicated for 24 hours prior to plating, and maintained in drug/vehicle during the plating process. One hour before the experiment, cells were washed with prewarmed RPMI-1640 and changed into fresh RPMI-1640 medium. Three baseline measurements were taken for oxygen consumption rate, followed by three measurements after injection of Rotenone (final concentration 20 uM) and Antimycin (20 uM). Following measurements, each cells from each well were counted for normalization. Basal oxygen consumption rate was measured by average of baseline measurements minus average of measurements following Rotenone/antimycin treatment.

Metabolite Consumption/Production Rates

50,000 cells per condition were plated in 5 cm dishes and allowed to adhere overnight. Media was changed the following day, with drug/vehicle treatments as indicated. 24 hours later, a representative sample from each condition was counted. Media was changed

for remaining samples. After an additional 24 hours, media was collected following centrifugation (800g*5min) to pellet debris, and final cell counts were measured. Glucose, lactate and glutamine concentrations in media were measured using YSI 2900 bioanalyzer as previously reported [27].

NAD Cofactor Measurement

For NAD cofactor measurements of cells growing in tissue culture, 30,000 cells per condition were plated in each well of a 6-well plate and allowed to adhere overnight. Cells were pretreated for 24 hours prior to plating in conditions of ACY1215/vehicle treatment. 4 hours prior to harvest, cells were washed 3X with prewarmed RPMI-1640 media and changed into 3 mL fresh media. Cells were washed 2X with chilled PBS followed by extraction with 200 uL of chilled lysis buffer (1% dodecyltrimethylammonium bromide [DTAB] in 0.2 N of NaOH diluted 1:1 with PBS). Samples were either directly used or flash frozen in liquid nitrogen, stored at −80°C, and thawed on ice prior to subsequent analysis. NAD+/NADH-Glo Assay (Promega G9072) and NADP+/NADPH-Glo Assay (Promega G9081) were used with slight modification to manufacturers protocol as described previously [28]. For NAD+/NADP+ measurements, 30 uL of lysate was diluted with 30 uL of lysis buffer and 30 uL of 0.4N HCl and incubated for 15 minutes at 60°C and neutralized by the addition of 30 uL 0.5M Tris base. For NADH/NADPH measurements, 30 uL of lysate was diluted with 30 uL of lysis buffer and incubated for 30 minutes at 75°C and neutralized by addition of 60 uL of 0.25M Tris base and 0.2N HCl. The remainder of the protocol was followed per manufacturer instructions for both kits to measure NAD+, NADH, NADP+, NADPH based on luminometry (Tecan M200) using a standard curve of serial dilution from reference sample to ensure linear range for measurements. NAD+, NADH, NADP+, NADPH measurements were normalized to cell counts measured at time of sample harvest.

For NAD cofactor measurements from tumor models, 10–20 mg of tumor pulverized in liquid nitrogen with chilled mortar and pestle was extracted in chilled lysis buffer at a volume of 200 μL per 10 mg tumor weight. Samples were vortexed at 4°C for 10 minutes, followed by centrifugation >20,000g for 10 minutes. Supernatant was transferred to fresh microcentrifuge tube and analysed as described above.

Glutathione Measurement

For glutathione measurements of cells growing in tissue culture, 3,000 cells per condition were plated in each well of flat-bottom, opaque white 96 well plate and allowed to adhere overnight. Cells were pretreated for 24 hours prior to plating in conditions of ACY1215/vehicle treatment. Media was gently aspirated, and samples were processed in plate using GSH/GSSG-Glo Assay (Promega V6611) according to manufacturer instructions. Luminometry measurements (Tecan M200) were normalized to cell counts determined at the time of plate measurement.

For glutathione measurements from tumor models, 10–20 mg of tumor pulverized in liquid nitrogen with chilled mortar and pestle was extracted in HPLC-grade methanol and dried over gaseous nitrogen. Dried metabolite pellets were resuspended in HPLC grade water at concentration of 10 mg original tumor input per mL of water. 5 and 10 μL of resuspension

(corresponding to 50 and 100 μg of extracted tumor) was transferred to 96 well plate and further processed per manufacturer instructions.

LC-MS Metabolite Measurement

50,000 cells were plated in 5 cm dish and allowed to adhere overnight. Cells were pretreated for 24 hours prior to plating in conditions of ACY1215/vehicle treatment. Media was changed the following day, with drug/vehicle treatments as indicated. 24 hours later, samples were washed 3X with prewarmed RPMI-1640 media 4 hours prior to harvest and changed into fresh to media. Cells were washed 2X with chilled, phosphate-free blood bank saline and extracted in 250 uL HPLC-grade 80% MeOH/20% H_2O (Sigma) with U-^{13}C-labeled amino acid standards [250 nM]. Samples were vortexed in 4°C cold room for 10 minutes before pelleting insoluble material via centrifugation. Polar metabolites from supernatant were dried under LN_2, and stored at −80°C prior to analysis.

On day of analysis, dried metabolites were resuspended in HPLC grade H2O. Metabolites were measured by LCMS on a QExactive bench top orbitrap mass spectrometer equipped with an Ion Max source and a HESI II probe, which was coupled to a Dionex UltiMate 3000 HPLC system (Thermo Fisher Scientific, San Jose, CA). External mass calibration was performed using the standard calibration mixture every 7 days. For each sample, 4 μL of each sample was injected onto a SeQuant® ZIC®-pHILIC 150 × 2.1 mm analytical column equipped with a 2.1 × 20 mm guard column (both 5 mm particle size; EMD Millipore). Buffer A was 20 mM ammonium carbonate, 0.1% ammonium hydroxide; Buffer B was acetonitrile. The column oven and autosampler tray were held at 25°C and 4°C, respectively. The chromatographic gradient was run at a flow rate of 0.150 mL/min as follows: 0–20 min: linear gradient from 80–20% B; 20–20.5 min: linear gradient form 20–80% B; 20.5–28 min: hold at 80% B. The mass spectrometer was operated in full-scan, polarity-switching mode, with the spray voltage set to 3.0 kV, the heated capillary held at 275°C, and the HESI probe held at 350°C. The sheath gas flow was set to 40 units, the auxiliary gas flow was set to 15 units, and the sweep gas flow was set to 1 unit. MS data acquisition was performed in a range of m/z = 70–1000, with the resolution set at 70,000, the AGC target at 1 × 106, and the maximum injection time (Max IT) at 20 msec. Relative metabolite quantification was performed in XCaliber QuanBrowser version 2.2 (ThermoFisher Scientific) with 5 ppm mass tolerance and a referencing in-house library of chemical standards.

Statistical Analysis

Statistical analysis was performed using GraphPad Prism 7 (GraphPad Software, San Diego, CA) unless stated otherwise. The IC_{50} for the dose-dependent curves following drug treatments was calculated using linear regression curve fit (log inhibition versus normalised response). Unless otherwise indicated, significance between two groups was determined using an unpaired two – tailed *t* test. For all statistical analysis, differences were considered to be statistically significant at *P<0.05, **p<0.01, and ***P<0.001.

Supplementary Material

Refer to Web version on PubMed Central for supplementary material.

Acknowledgements:

We thank members of the Experimental Pathology Research Laboratory, which is partially supported by the Cancer Center Support Grant P30CA016087 at NYU Langone's Laura and Isaac Perlmutter Cancer Center. This work is supported by a Young Investigator Award from the ASCO Conquer Cancer Foundation and AACR-Bristol-Myers Squibb Immuno-oncology Research Fellowship (CSN)

Funding:

This work was supported by the NCI grants (ROICA219670, PO1CA15430) (KKW) and the H2020 MSCA Global Fellowship (799724) (CMD).

References

1. Ferrarelli LK. HDAC inhibitors in solid tumors and blood cancers. Science Signaling 2016;9:ec216–ec216.
2. Yau HL, Ettayebi I, De Carvalho DD. The cancer epigenome: exploiting its vulnerabilities for immunotherapy. Trends in cell biology 2019;29:31–43. [PubMed: 30153961]
3. Laino AS, Betts B, Veerapathran A, et al. HDAC6 selective inhibition of melanoma patient T-cells augments anti-tumor characteristics. Journal for immunotherapy of cancer 2019;7:33. [PubMed: 30728070]
4. Dowling CM, Hollinshead KER, Di Grande A, et al. Multiple screening approaches reveal HDAC6 as a novel regulator of glycolytic metabolism in triple-negative breast cancer. Science Advances 2021;7:eabc4897. [PubMed: 33523897]
5. Chen Z, Cheng K, Walton Z, et al. A murine lung cancer co-clinical trial identifies genetic modifiers of therapeutic response. Nature 2012;483:613–617. [PubMed: 22425996]
6. Gu M, Xu T, Chang P. KRAS/LKB1 and KRAS/TP53 co-mutations create divergent immune signatures in lung adenocarcinomas. Therapeutic Advances in Medical Oncology 2021;13:17588359211006950. [PubMed: 33995590]
7. Skoulidis F, Goldberg ME, Greenawalt DM, et al. STK11/LKB1 mutations and PD-1 inhibitor resistance in KRAS-mutant lung adenocarcinoma. Cancer discovery 2018;8:822–835. [PubMed: 29773717]
8. Garcia D, Shaw RJ. AMPK: Mechanisms of Cellular Energy Sensing and Restoration of Metabolic Balance. Molecular cell 2017;66:789–800. [PubMed: 28622524]
9. Shackelford DB, Abt E, Gerken L, et al. LKB1 inactivation dictates therapeutic response of non-small cell lung cancer to the metabolism drug phenformin. Cancer Cell 2013;23:143–158. [PubMed: 23352126]
10. Bhatt V, Khayati K, Hu ZS, et al. Autophagy modulates lipid metabolism to maintain metabolic flexibility for Lkb1-deficient Kras-driven lung tumorigenesis. Genes Dev 2019;33:150–165. [PubMed: 30692209]
11. Gillette MA, Satpathy S, Cao S, et al. Proteogenomic Characterization Reveals Therapeutic Vulnerabilities in Lung Adenocarcinoma. Cell 2020;182:200–225.e235. [PubMed: 32649874]
12. Kim J, Hu Z, Cai L, et al. CPS1 maintains pyrimidine pools and DNA synthesis in KRAS/LKB1-mutant lung cancer cells. Nature 2017;546:168–172. [PubMed: 28538732]
13. Dowling CM, Hollinshead KE, Di Grande A, et al. Multiple screening approaches reveal HDAC6 as a novel regulator of glycolytic metabolism in triple-negative breast cancer. Science advances 2021;7:eabc4897. [PubMed: 33523897]
14. Liu Y, Marks K, Cowley GS, et al. Metabolic and functional genomic studies identify deoxythymidylate kinase as a target in LKB1-mutant lung cancer. Cancer Discov 2013;3:870–879. [PubMed: 23715154]
15. Son J, Lyssiotis CA, Ying H, et al. Glutamine supports pancreatic cancer growth through a KRAS-regulated metabolic pathway. Nature 2013;496:101–105. [PubMed: 23535601]
16. Davidson SM, Papagiannakopoulos T, Olenchock BA, et al. Environment impacts the metabolic dependencies of Ras-driven non-small cell lung cancer. Cell metabolism 2016;23:517–528. [PubMed: 26853747]

17. Son J, Lyssiotis CA, Ying H, et al. Glutamine supports pancreatic cancer growth through a KRAS-regulated metabolic pathway. Nature 2013;496:101–105. [PubMed: 23535601]
18. Ying H, Kimmelman AC, Lyssiotis CA, et al. Oncogenic Kras maintains pancreatic tumors through regulation of anabolic glucose metabolism. Cell 2012;149:656–670. [PubMed: 22541435]
19. Sayin VI, LeBoeuf SE, Singh SX, et al. Activation of the NRF2 antioxidant program generates an imbalance in central carbon metabolism in cancer. Elife 2017;6.
20. Muir A, Danai LV, Gui DY, et al. Environmental cystine drives glutamine anaplerosis and sensitizes cancer cells to glutaminase inhibition. Elife 2017;6.
21. McCormick F KRAS as a therapeutic target. Clinical Cancer Research 2015;21:1797–1801. [PubMed: 25878360]
22. Rosell R, Aguilar A, Pedraz C, et al. KRAS inhibitors, approved. Nature Cancer 2021;2:1254–1256. [PubMed: 35121930]
23. Skoulidis F, Li BT, Dy GK, et al. Sotorasib for lung cancers with KRAS p. G12C mutation. New England Journal of Medicine 2021;384:2371–2381. [PubMed: 34096690]
24. Awad MM, Liu S, Rybkin II, et al. Acquired resistance to KRASG12C inhibition in cancer. New England Journal of Medicine 2021;384:2382–2393. [PubMed: 34161704]
25. Dobin A, Davis CA, Schlesinger F, et al. STAR: ultrafast universal RNA-seq aligner. Bioinformatics 2013;29:15–21. [PubMed: 23104886]
26. Li B, Dewey CN. RSEM: accurate transcript quantification from RNA-Seq data with or without a reference genome. BMC Bioinformatics 2011;12:323. [PubMed: 21816040]
27. Hosios AM, Hecht VC, Danai LV, et al. Amino Acids Rather than Glucose Account for the Majority of Cell Mass in Proliferating Mammalian Cells. Dev Cell 2016;36:540–549. [PubMed: 26954548]
28. Gui DY, Sullivan LB, Luengo A, et al. Environment Dictates Dependence on Mitochondrial Complex I for NAD+ and Aspartate Production and Determines Cancer Cell Sensitivity to Metformin. Cell Metab 2016;24:716–727. [PubMed: 27746050]

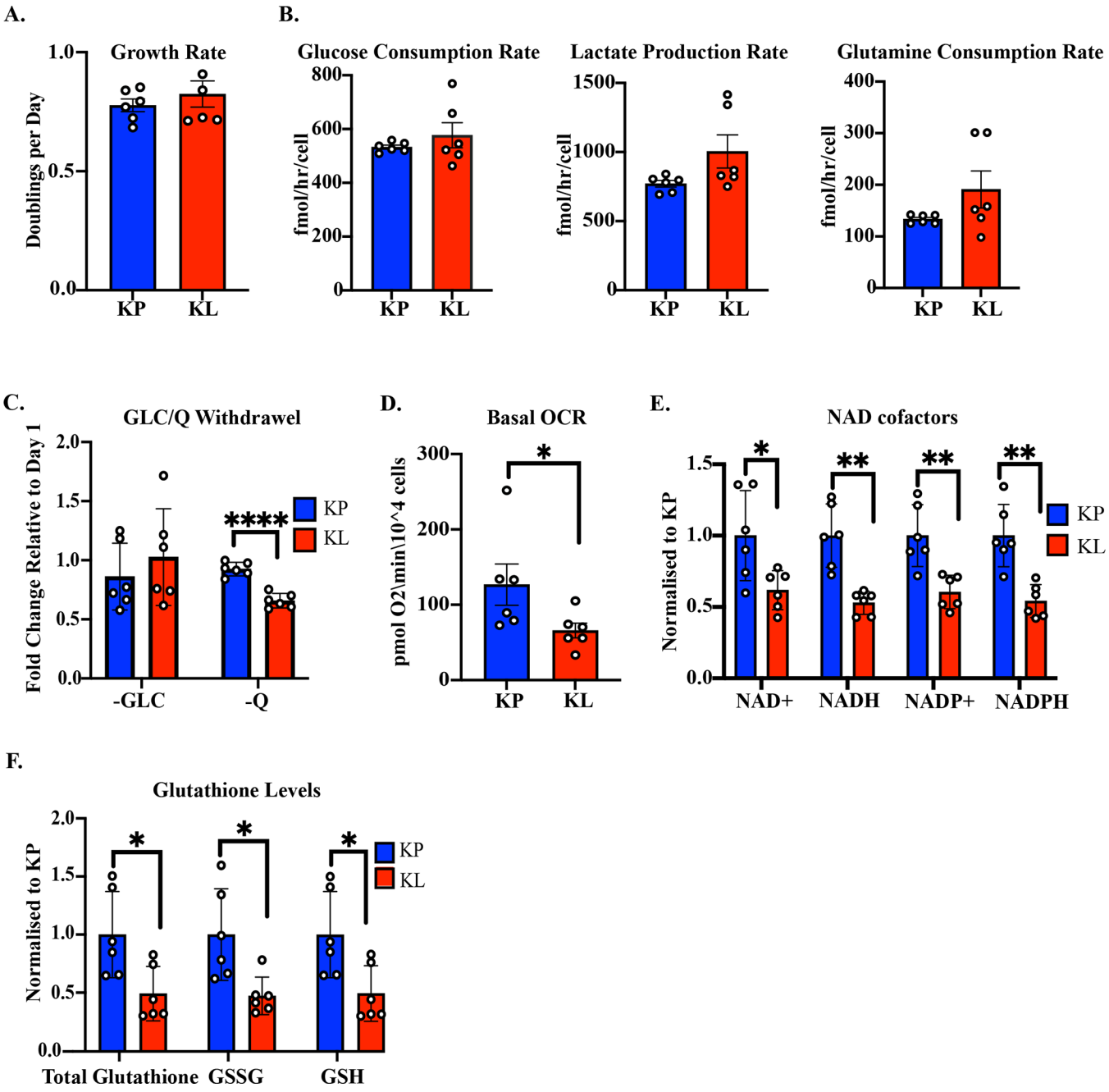

Figure 1: Evaluation of metabolic differences between KRAS/TP53 and KRAS/LKB1 comutant cells.

(A) Growth rate, indicated as doublings per day. **(B)** Glucose, glutamine consumption and lactate production in media conditioned during cell growth. **(C)** Growth rate under conditions of glucose and glutamine withdrawal. **(D)** Basal oxygen consumption rate. **(E)** NAD co-factor levels, normalized to cell counts and referenced to mean of KP condition. **(F)** Total, oxidized, and reduced glutathione levels, normalized to cell counts and referenced to mean of KP condition. For each figure, each data point represents the average of 2–3 biological replicates. Three distinct cell lines were used from each genotype, and the

results of two representative experiments are shown. Statistical analysis was performed with unpaired, parametric student's T-test. For all panels, P-values noted as follows: *P<0.05, **P<0.01****P<0.0001.

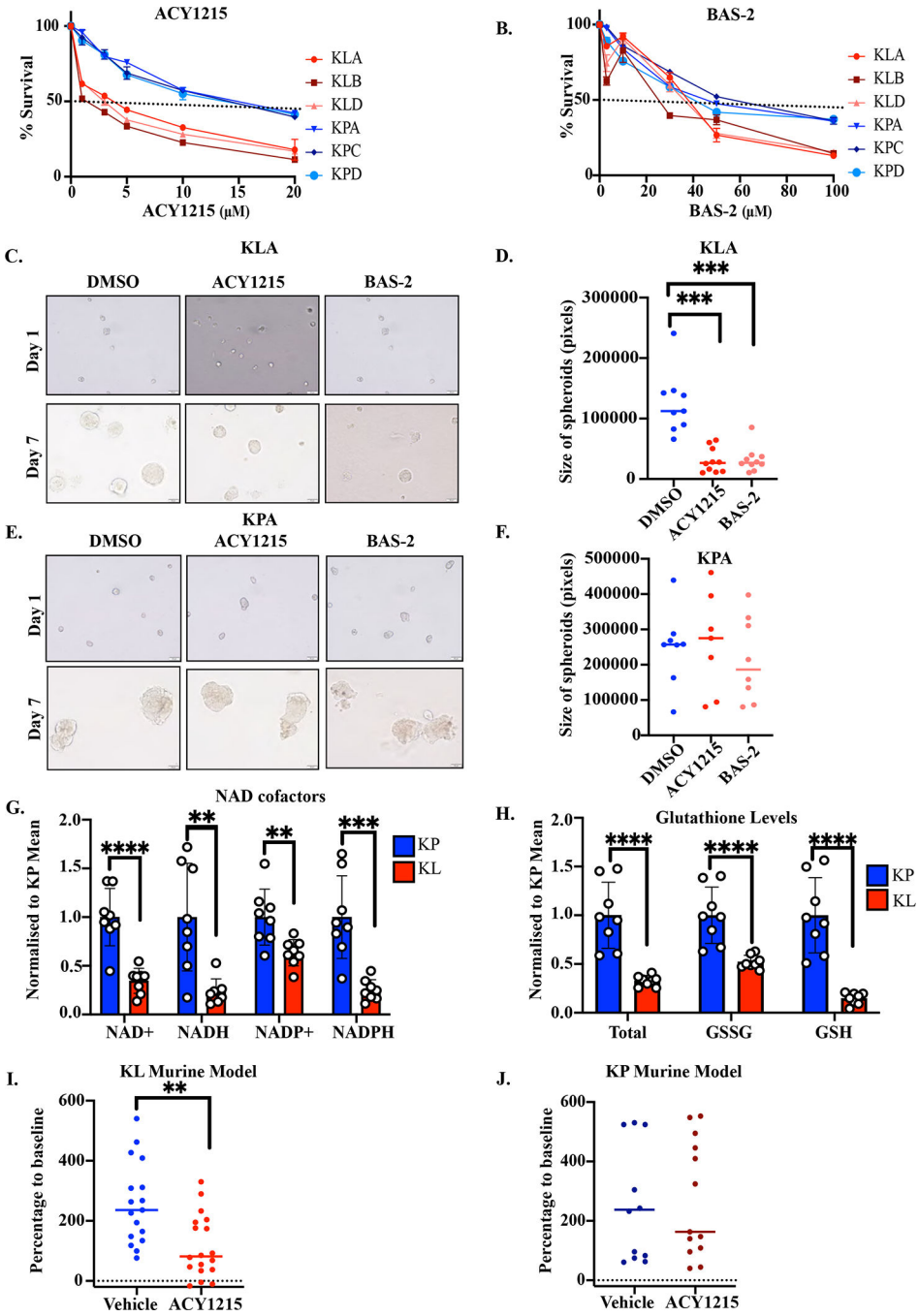

Figure 2: KRAS/LKB1 models demonstrate enhanced sensitivity to HDAC6 inhibition.

(A) Dose response of a panel of KL and KP NSCLC murine cell lines to ACY1215 as measured by CCK8 cell death assay (n=3, mean +/− SEM) (IC50 Values; KLA 3.4μM, KLB 1.9μM, KLC 2.8μM, KPA 14.2μM, KPC 12.7μM, KPD 12.3μM). **(B)** Dose response of a panel of KL and KP NSCLC murine cell lines to BAS-2 as measured by CCK8 cell death assay (n=3, mean +/− SEM) (IC50 Values; KLA 33.2μM, KLB 23.1μM, KLC 30.6μM, KPA 48.2μM, KPC 59.1μM, KPD 41.2μM). **(C)** Images of KLA cells grown in Matrigel for 7 days following treatment with 1μM of ACY1215 or 10μM of BAS-2 (n=3).

(D) Scatter dot plot shows the size of spheroids in all treatment groups **(E)** Images of KPA cells grown in Matrigel for 7 days following treatment with 1μM of ACY1215 or 10μM of BAS-2 (n=3). **(F)** Scatter dot plot shows the size of spheroids in all treatment groups. **(G)** NAD co-factor levels and **(H)** Glutathione levels in in subcutaneous tumors derived from implantation of KLA and KPA murine cancer cell lines. **(I&J)** C57BL/6 mice were subcutaneously inoculated with 1×10^6 KL **(I)** or KP **(J)** cells and following tumor formation were treated with 50mg/kg of ACY1215 or vehicle control for 7 days. Tumors were measured and plotted as percentage change in tumor size following treatment. Statistical analysis was performed with unpaired, parametric student's T-test. For all panels, P-values noted as follows: **P<0.01,***P<0.001.

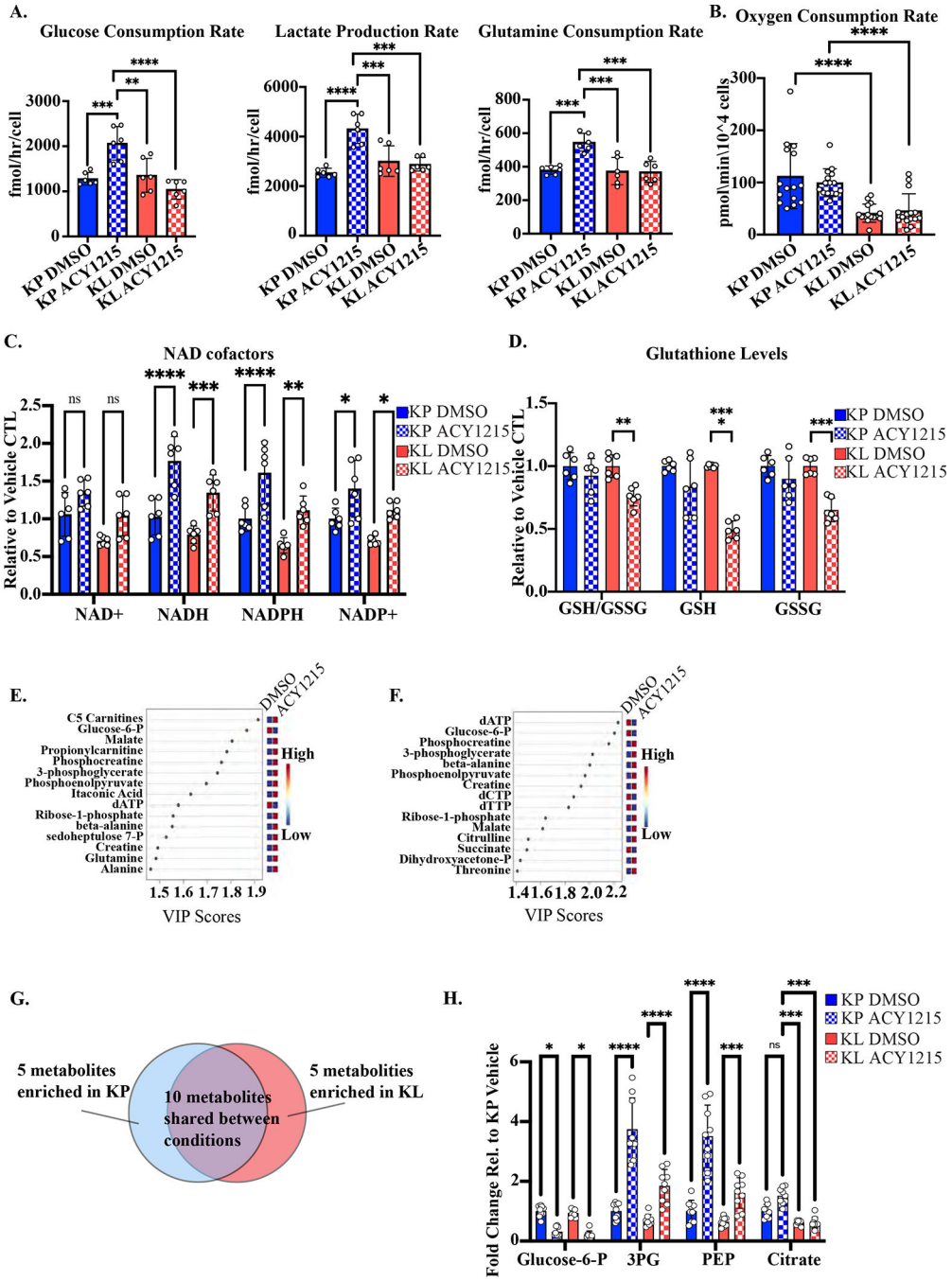

Figure 3: Metabolic alterations associated with pharmacologic HDAC6 inhibition

Cells were treated with ACY1215 1 uM or 0.01% DMSO Vehicle control for 24 hours before making the following metabolic assessments: **(A)** Glucose, glutamine consumption and lactate production. **(B)** Basal oxygen consumption rate. **(C)** NAD co-factor levels, normalized to cell counts and referenced to mean of KP condition. **(D)** Total, oxidized, and reduced glutathione levels, normalized to cell counts and referenced to mean of KP condition. **(E)** Variable importance projection of differential enrichment of metabolites measured by LC/MS in the KP background, comparing 24 hour ACY1215 1uM versus

0.01% DMSO control. **(F)** Same analysis in the KL background. **(G)** Venn diagram illustrating overlap of metabolites identified through VIP. **(H)** Relative metabolite levels for glucose-6-phosphate, 3-phosphoglycerate, phosphoenolpyruvate and citrate, as normalized to the vehicle-treated KP condition. For each figure, each data point represents the average of 2–3 biological replicates. Three distinct cell lines were used from each genotype, and the results of two representative experiments are shown. For panels A and B, statistical analysis was performed with one-way ANOVA with Tukey's multiple comparisons test. For panels C, D, and H, statistical analysis was performed with two-way ANOVA with Tukey's multiple comparisons test. For all panels, P-values noted as follows: *P<0.05, **P<0.01,***P<0.001, ****P<0.0001.

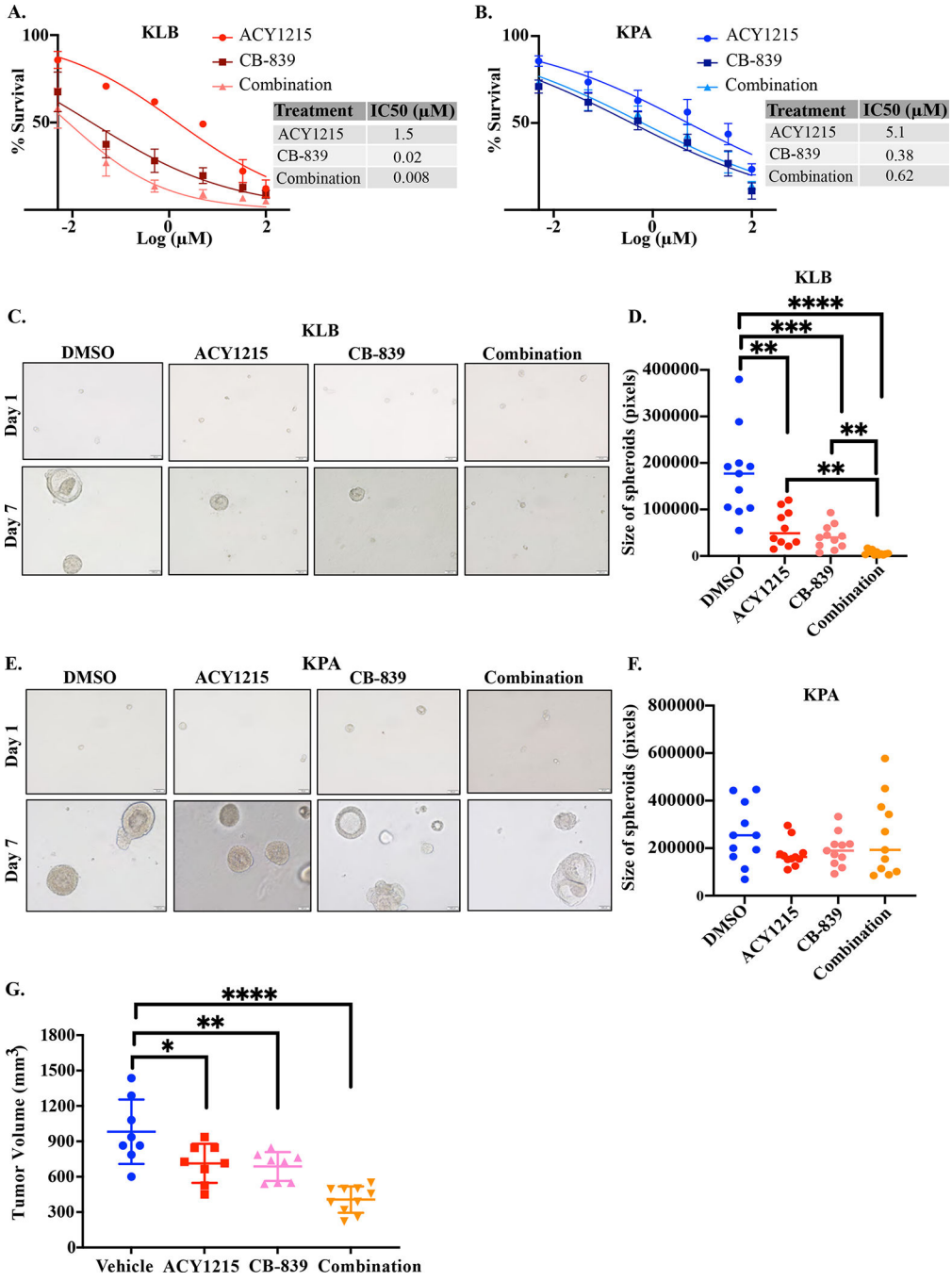

Figure 4: Enhanced efficacy of combining HDAC6 inhibitors with Glutaminase inhibitors in KRAS/LKB1 NSCLC modes.

(A&B) Dose response of KLB **(A)** and KPA **(B)** NSCLC murine cell lines to ACY1215, CB-839 and combinations as measured by CCK8 cell death assay (n=3, mean +/− SEM, drug concentration is Log_{10}). **(C)** Images of KLB cells grown in Matrigel for 7 days following treatment with 1μM of ACY1215, 50nM CB-839 or combination (1μM of ACY1215 & 50nM CB-839) (n=3). **(D)** Scatter dot plot shows the size of KLB spheroids in all treatment groups. **(E)** Images of KPA cells grown in Matrigel for 7 days following

treatment with 1μM of ACY1215, 50nM CB-839 or combination (1μM of ACY1215 & 50nM CB-839) (n=3). **(F)** Scatter dot plot shows the size of KPA spheroids in all treatment groups. **(G)** C57BL/6 mice were subcutaneously inoculated with 1×10^6 KL cells and following tumor formation were treated with vehicle, ACY1215 (50mg/kg), CB-839 (200mg/kg) or combination for 14 days. At the end of the experiment mice were culled and tumors volume was measured [(length × width^2)/2]. Statistical analysis for 3D spheroids was performed with unpaired, parametric student's T-test. Statistical analysis for mouse models was performed with one-way anova, Dunnett's multiple comparisons. For all panels, P-values noted as follows: *P<0.05, **P<0.01,***P<0.001, ****P<0.0001.